INNOVATIVE DESIGN OF ROTARY TILL BLADES TO REDUCE CUTTING RESISTANCE
/
仿生设计模仿棕熊爪的旋转叶片以降低土壤切割阻力

Kai ZHAO[1)], Huili ZHANG*[1)], Ahmed F. EL-SHAFIE[2)3)], Xiaoshuai ZHENG[4)], Zhengping LI [5)], Shuai ZHENG[1)], Zhipeng SUN[1)]

[1)] College of Mechanical and Electrical Engineering, Qingdao Agricultural University, Qingdao, China;
[2)] National Center of Technology Innovation for Comprehensive Utilization of Saline-Alkali Land, Dongying, China;
[3)] Water relations and Field Irrigation Department, National Research Centre; Cairo, Egypt;
[4)] College of Mechanical and Automotive Engineering, Qingdao University of Technology; Qingdao, China;
[5)] Yellow River Delta Intelligent Agricultural Machinery Equipment Industry Academy, Dongying, China
Tel: +86 13605424499; E-mail: zhhuili73@163.com
Corresponding author: Zhang huili

DOI: https://doi.org/10.35633/inmateh-78-63

Keywords: *brown bear claw; biomimetic design; rotary blade; DEM; saline-alkali land*

ABSTRACT
Rotary tillage in cohesive, salt-affected soils requires significant energy, making the optimization of blade geometry essential to reduce resistance. This study takes inspiration from the digging claw of the brown bear (Ursus arctos) to design a bio-inspired rotary blade and assess its performance using a calibrated discrete element method (DEM) model and soil bin experiments. The DEM model was specifically calibrated for the salt-affected soils of the Yellow River Delta. Key parameters for the study were identified using a Plackett-Burman test and optimized through a central composite design, with experimentally measured draft force as the response variable. The performance of the bio-inspired blade was compared to that of a conventional IT-type blade, focusing on torque demand and soil fragmentation. Simulation results indicated that the bio-inspired blade reduced torque by up to 13% across a rotational speed range of 160-320 RPM and by up to 11% at tillage depths of 60-140 mm. Soil bin tests reinforced these findings, showing that the bio-inspired blade required 17.8% less torque than the IT-type blade. However, the IT-type blade achieved a slightly higher soil fragmentation rate, exceeding the bio-inspired design's performance by 3.9%. This study demonstrates that biomimetic design can significantly reduce energy requirements for rotary tillage while maintaining effective soil fragmentation.

摘要
旋耕作业属于高能耗工序，尤其在黏性盐渍土壤中更为显著。因此，优化耕刀几何结构对降低土壤抗剪切阻力、提升耕作效率至关重要。受自然界生物结构启发的仿生设计，为实现这一优化提供了可行方案。本研究基于棕熊爪（Ursus arctos）的轮廓曲线设计了仿生耕刀。采用离散元法（DEM）模型并进行校准，以精确模拟黄河三角洲特定土壤条件下的土-刀具相互作用。通过校准模型评估仿生旋耕刀的性能表现。首先通过 Plackett-Burman 筛选试验确定 DEM 模型的关键参数，随后采用中心复合设计法，以凿柄实验测得的拉力作为校准响应，确定参数最优组合。通过 DEM 模拟和土壤箱实验，将仿生耕刀与传统 IT 型耕刀的性能进行对比，主要以扭矩需求和土壤破碎率作为评估指标。数值积分采用梯形法则计算扰动土体面积。模拟结果显示，仿生叶片产生的扭矩显著降低，在 160 至 320 转/分钟的转速范围内降幅可达 13%，在 60-140 毫米耕作深度时降幅最高达 11%。土壤箱测试表明，仿生叶片产生的旋转扭矩比 IT 型叶片低 17.8%。相比之下，IT 型叶片的土壤破碎率略高，比仿生叶片高出 3.9%。本研究证明，仿生设计原则（特别是源自挖掘适应性生物结构的设计）能在保持农业效能的同时，大幅降低旋耕工具的能量需求。此外，经过校准的离散元模型框架为未来研究黄河三角洲盐渍化土壤中的土-机相互作用提供了可靠工具，为开发适用于复杂土壤的节能机械提供了支持。

INTRODUCTION
The global need to improve soil-engaging tools is highlighted by a significant amount of research across various agricultural settings. Studies have shown that soil compaction caused by machinery traffic is a widespread issue, negatively affecting soil structure and crop growth (*Ungureanu et al., 2015*). This concern has driven current trends in the design and selection of deep tillage equipment, focusing on reducing soil degradation (*Vlăduțoiu et al., 2017*).

The importance of efficient tillage is even more pronounced in areas with heavy or challenging soils, where specialized tools are essential for proper seedbed preparation (*Vlăduț et al., 2018*). At the same time, the implementation of conservation agriculture systems, such as minimum-till and no-till practices, has been thoroughly examined as a strategic method to lower costs, improve soil quality, and reduce machinery traffic. This, in turn, decreases fuel consumption and labor requirements (*Bularda et al., 2020*). Recently, research has also focused on the tribological aspects of tillage tools, investigating the wear mechanisms of chisel knives to enhance their durability and performance (*Vlăduțoiu et al., 2023*). Overall, these studies represent a continuous and comprehensive effort to promote the sustainability and effectiveness of tillage practices.

Rotary tillage improves agricultural conditions by breaking up and turning over the top layer of soil. This process enhances soil structure, increases water permeability and retention, and helps incorporate plant residue *(Chen et al., 2024)*. As a result, it creates a better environment for crop growth, promoting seed germination and root development *(Chertkiattipol et al., 2010; Siddique et al., 2012; Xiong et al., 2017; Xiong et al., 2018)*. The key parameters affecting the draft and vertical forces of tillage tools include the tool's geometry, working depth, soil properties, and the associated soil failure pattern *(Godwin et al., 2007)*. Since rotary blades directly interact with the soil, their geometric design is crucial for reducing energy consumption and ensuring effective tillage operation *(Li et al., 2023; Zheng et al., 2025)*. Therefore, optimizing the geometric structure of rotary blades is a crucial area of research in agricultural machinery. *Hao et al., (2019)* designed a wedge-shaped rotary blade and evaluated its performance in soil bin tests. Their findings revealed that across the tested operational parameters, the wedge-shaped blade reduced average rotational resistance torque by 11.35% and average power consumption by 9% compared to a conventional blade. Additionally, the modified design improved the soil fragmentation rate by 4%.

The superior ability of some animals to dig and burrow in soil has inspired researchers in agricultural machinery to adopt bionic principles in the design of soil-engaging components that achieve high operational performance while reducing soil-cutting resistance *(Sun et al., 2018; Salem et al., 2021)*. *El Salem et al., (2023)* investigated the impact of integrating a bio-inspired convex surface geometry, specifically, a micro-convex structure modeled after dung beetle skin, with a low-surface-energy polymer, ultra-high molecular weight polyethylene (UHMW-PE), on soil-tool adhesion and sliding resistance. Their comprehensive soil bin experiments were conducted across various soil textures (silty clay and sandy clay loam), moisture contents (18–33% on a dry basis), and sliding speeds (0.15–0.3 m/s). The results demonstrated that the domed UHMW-PE surface significantly reduced both soil adhesion and sliding resistance under all tested conditions compared to a conventional flat carbon steel plate. The authors attributed this enhanced performance to the combined effects of the biomimetic surface structure, which disrupts the interfacial water film, and the polymer coating's inherent hydrophobic properties. They concluded that this integrated bio-inspired and materials-based approach offers a promising strategy for developing more efficient soil-engaging tools. In the same context, a bioinspired rotary blade was designed based on the contour curves of the forefoot toes of Gryllotalpa orientalis to reduce energy consumption. DEM simulations and soil bin experiments revealed that, compared to the IT245 Chinese standard blade, the bionic design decreased maximum horizontal resistance by up to 9.91% and vertical resistance by up to 9.74% at speeds ranging from 150 to 250 r/min. Additionally, the average torque was reduced by up to 10.53%. This study demonstrates that using a biomimetic approach effectively lowers working resistance and energy demand during rotary tillage *(Yang et al., 2019)*.

Rotary tillers mainly use three types of blades: IT-type (ITTB), L-type (LTB), and J-type (JTB). Each blade consists of three functional regions: the lengthwise, curved, and sidelong parts. During tillage, these components interact with the soil through a combination of impact, compression, and cutting actions, leading to significant tillage resistance and, consequently, high energy consumption *(Cheng et al., 2023)*. To tackle this issue, the current study aims to: (1) design and fabricate a bioinspired rotary blade optimized for reduced soil-cutting resistance; and (2) propose and calibrate a discrete element method (DEM) model that reliably simulates soil-tool interactions under the salt-affected soil conditions typical of the Yellow River Delta. The performance of the proposed blade was assessed using the calibrated DEM model and validated through soil bin tests, with rotating resistance torque and soil fragmentation rate being the primary evaluation metrics.

MATERIALS AND METHODS

1. Detection and extraction of geometric features from the bionic prototype

Brown bears (Ursus arctos) have strong claws that typically measure between two to four inches in length and are gently curved.

This claw shape is particularly well-suited for digging up roots and creating dens in hard soil. Inspired by the brown bear's effective digging abilities, this study uses its claw as a bionic prototype for the design of a novel rotary tiller blade. Edge detection and morphological analysis of the bionic prototype's front claw were conducted using mathematical morphology within MATLAB's Image Processing Toolbox. These techniques operate on the standard digital image representation, which is a discrete two-dimensional matrix of size M × N (or a three-dimensional stack for RGB images). This data structure enables direct application of morphological structuring elements and convolution kernels, leveraging MATLAB's optimized matrix-based computational framework for efficient image processing *(Zhihong et al., 2018)*. Edge extraction for the bionic prototype was performed using a multi-stage protocol (Figure 1).

The workflow initiates with a raw RGB image and proceeds through several stages: conversion to grayscale, binarization, and morphological operations such as dilation and erosion. This is followed by hole filling and edge detection using the Canny algorithm. Next, the edges are digitized, and polynomial curve fitting is applied to the contours. The process concludes with the creation of a digital 3D model. The Canny algorithm was used to create an accurate edge map, thanks to its multi-step process that includes noise reduction, gradient calculation, non-maximum suppression, and hysteresis thresholding. The bionic prototype features two main contours that define its edges: an inner edge outlining the soil-engaging surface and an outer edge following the dorsal profile (Figure 2). The digitized pixel coordinates for both the inner and outer contours are shown in Figure 3, along with their corresponding best-fit polynomial equations. The outer edge is represented by a sixth-order polynomial, while the inner edge is described by a fourth-order polynomial, along with their respective coefficients of determination.

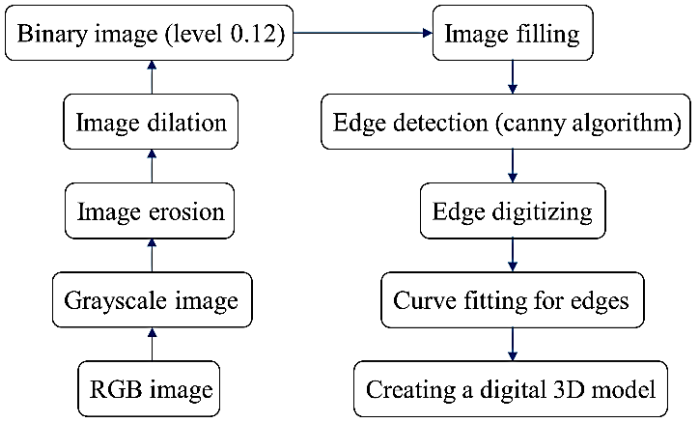

Fig. 1 - Flowchart illustrating the multi-stage image processing workflow for the edge detection and extraction of the brown bear claw

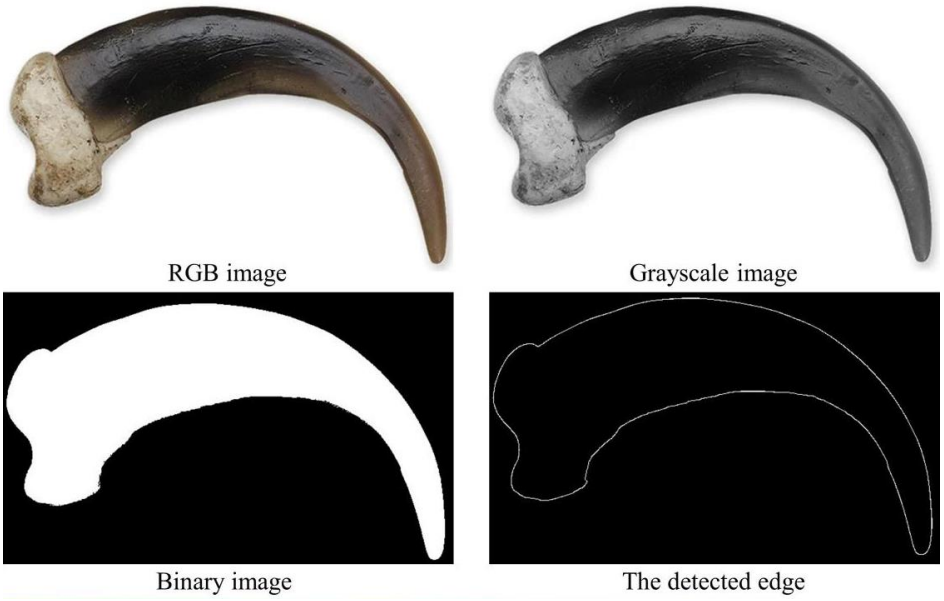

Fig. 2 - Edge extraction results from the brown bear claw image show the transition from the original RGB image to grayscale, then to binary, and finally to the detected edges

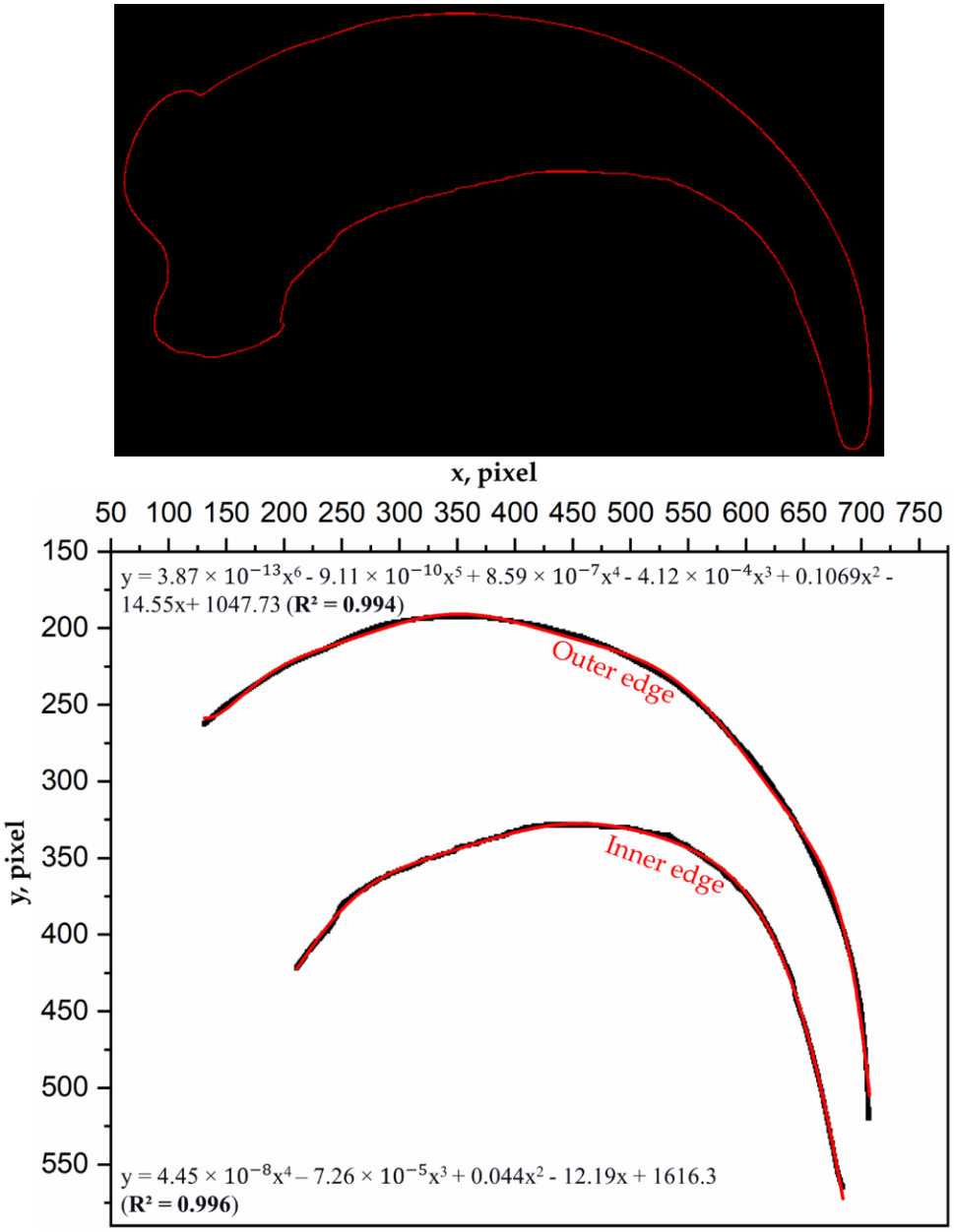

Fig. 3 - Digitizing and applying polynomial curve fitting to the contours of brown bear claws

2. Design of the Bio-inspired Rotary Blade

During tillage, the blade cuts through soil while incorporating grass stems and crop residues. Given these demanding functions, the rotary tiller is one of the most energy-intensive soil-engaging tools *(Xie et al., 2025)*. To reduce the high operational resistance encountered with traditional blade designs, this study presents a biomimetic optimization of the rotary blade, based on the contour curves of the brown bear's claw. The two-dimensional fitting curves of the bear's front claw, obtained previously, were extruded by 11 mm along the z-axis using the ANSYS SpaceClaim modeling tool to create a three-dimensional model of the claw contour curves (Figure 4a). Based on biomechanical observations of how bear claws interact with soil during digging, where the main contact happens below the claw's convex area *(Li et al., 2016)*, Therefore, to adapt the three-dimensional claw model to the functional geometry of a rotary blade, the portion above point F was trimmed, retaining only the segment that actively engages with the soil (Figure 4b). The trimmed claw model was then proportionally scaled to match the dimensional parameters (length, width, height, and radius) of a conventional IT-type rotary blade to ensure functional equivalence and comparable performance in the performance evaluation.

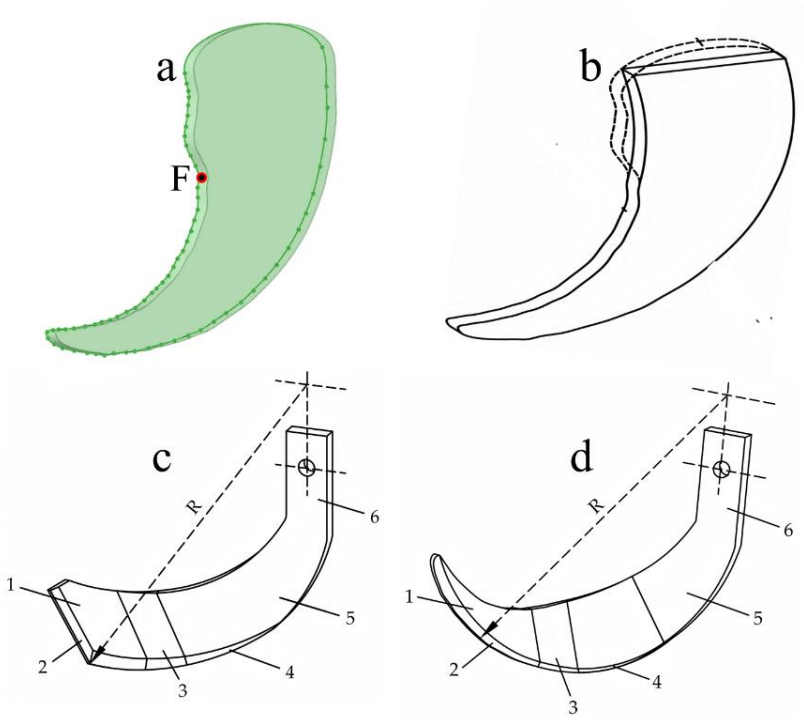

Fig. 4 - Bio-inspired rotary blade design based on brown bear claw morphology

(a) a simplified three-dimensional contour model of a brown bear claw for biomimetic translation, (b) a trimmed version of the model, (c) a conventional IT-type rotary blade serving as the reference design, and (d) the proposed bio-inspired rotary blade, which highlights key functional regions: (1) inner side, (2) sidelong part, (3) curved section, (4) side cutting edge, (5) lengthwise part, and (6) blade handle.

3. Soil Bin Test

A comparative study was conducted in a soil bin facility (Figure 5), comparing a conventional IT-type blade (used as the reference) with a bio-inspired rotary blade (Figure 6). The blade torque and soil fragmentation rate were used as evaluation indices in this study. The rotary implement is powered by a 7.5 kW motor, allowing it to operate at speeds ranging from 0 to 600 rpm. Real-time tillage torque is measured using a dynamic torque transducer with a capacity of 1000 N·m, which is installed on the motor's power take-off (PTO). To ensure that fresh soil is presented to the blade for each test run, the facility features a conveyor belt system that can transport soil to depths of up to 350 mm. The conveyor's linear speed can be adjusted between 0.05 and 1 m·s^{-1} beneath the fixed unit that houses the implement. Ten blades of each type, five left-handed and five right-handed, are mounted centrally on a 0.8 m shaft in a symmetrical double-spiral configuration to ensure balanced loading. The soil fragmentation rate, which is defined as the proportion of soil aggregates with a diameter of 10 mm or less, was determined following the protocol outlined in GB/T 24675.6-2021 ("Test Methods for Conservation Tillage Equipment – Part 6: Rotary Tillage Machinery"). Immediately after the rotary tillage blade passed through, soil samples were collected from the tilled layer at a depth of 0–100 mm using a steel frame sampler measuring 20 × 20 cm. To account for spatial variability within the soil bin, samples were taken from 10 randomly selected points and then combined to create a composite sample. The composite sample was carefully crumbled by hand along natural failure planes and air-dried until it reached a constant mass. A 2 kg sub-sample was then sieved through a standard sieve with a 10 mm aperture using a GZS-1 High-Frequency Sieve Shaker for 5 minutes. The mass of the soil fraction that passed through the 10 mm sieve and the mass retained on it were recorded. The dry soil fragmentation rate was calculated as the ratio of the mass of the aggregates measuring 10 mm or less to the total dry mass of the sub-sample, expressed as a percentage (Equation 1).

Given the controlled and homogeneous conditions inherent to soil bin testing, which ensure uniform soil preparation and tillage depth throughout the bin, this procedure was performed once for each test condition without replication.

$$\text{Soil Fragmentation Rate } (\%) = \frac{M_f}{M_t} * 100 \quad (1)$$

where M_f is the mass of soil fragments ≤ 10 mm and M_t is the total soil mass of the tilled layer sample.

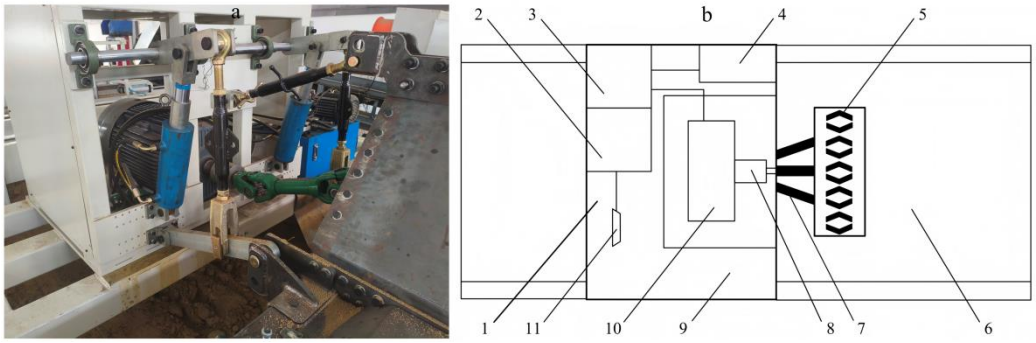

Fig. 5 - The soil bin test facility used for comparative blade evaluation

(a) Photograph of the operational setup. (b) Annotated schematic identifying the core subsystems: (1) fixed carriage, (2) data acquisition system, (3) motor control box, (4) hydraulic system, (5) tested blades, (6) conveyor belt, (7) three-point hitch, (8) torque sensor, (9) motor, and (10) control and monitoring computer.

Fig. 6 - Physical specimens of the tested rotary blades

(a) conventional IT-type blade; (b) bio-inspired rotary blade

4. Chiseling Experiments

Chiseling experiments were conducted in experimental fields located at the Yellow River Delta Intelligent Agricultural Machinery Equipment Industry Academy in Dongying, China (118° 39′ 9″ E, 37° 18′ 39″ N). The draft force of the chisel shank was measured using three S-shaped load cells (model SBT620TF; capacity: 1000 kg). The shank was attached to a 150-horsepower tractor (John Deere model 6E-1504-PL) using a standard three-point hitch (Figure 7).

Fig. 7 - Measurement of draft force for the chisel shank operating in cohesive, salt-affected soil in the Yellow River Delta: (a) experimental setup and (b) the resulting furrow profile

Before data collection, a 10-meter acceleration zone was established to allow the tractor to reach a steady operating speed *(Qin et al., 2025)*. During each chiseling pass, the draft force was continuously recorded using a multi-channel dynamic signal acquisition system (DH3820 N Distributed Stress-Strain Test and Analysis System, Donghua Testing Technology Co., China). The total net draft force (DF) in the direction of travel was calculated in real time by summing the horizontal force components from each sensor *(Md-Tahir et al., 2019)*. After the operation, the average tillage depth was determined by excavating and measuring the loosened soil at five equally spaced points along a 5-meter section of the furrow. The operating speed was calculated by timing the tractor over a fixed 30-meter travel distance within the test section. The experiment was conducted with five replicates. The resulting mean draft force, tillage depth, and operating speed were 712 ± 73 N, 220 ± 27 mm, and 0.94 ± 0.05 m/s, respectively. The measured draft force was then used as the calibration metric for key parameters in the proposed model.

5. Development, Calibration, and Implementation of the Discrete Element Model

This study aimed to develop and calibrate a suitable discrete element model to simulate soil-tool interaction under soil conditions in the Yellow River Delta (YRD).

This region is a young alluvial plain with a semi-humid continental monsoon climate and a high groundwater table, typically located 1.0 to 2.0 meters below the surface *(Fan et al., 2010)*. These conditions lead to consistently high soil moisture during soil preparation operations, particularly from June to September. In such moist environments, soil cohesion is influenced by interparticle forces, including liquid bridges and van der Waals forces *(El Salem et al., 2026)*, which present specific challenges for accurate simulation. To address these challenges, a combined hysteretic spring–linear cohesion contact model was employed, as described by *Ucgul et al., (2015)*.

The soil utilized in this study was collected from the tillage layer (0–200 mm depth) of a representative salt-affected field located in the reclamation region of the Yellow River Delta (YRD) in Dongying City, China. To establish a solid foundation for the subsequent calibration of a discrete element method (DEM) model, the physical and mechanical properties of the soil were characterized following standard laboratory procedures. The gravimetric moisture content was determined by oven-drying field-moist samples at 105°C for 24 hours until a constant mass was achieved. Water loss was then calculated relative to the final dry mass. Wet bulk density was measured using the core method, where undisturbed samples were collected in stainless steel cylinders (61.8 mm in diameter and 20 mm in height). The wet mass of the sample was divided by the core volume to obtain the bulk density. Soil cohesion was determined through direct shear tests on remolded samples that were compacted to the target wet bulk density and moisture content. The specimens were sheared under normal stresses of 12, 18, 24, 30, 40, and 50 kPa, following the procedure described by *Marsh and Rixon (1991)*. The resulting shear stresses were recorded to create a failure envelope based on the Mohr-Coulomb failure criterion. Particle size distribution was determined using sieve analysis for the coarser fractions and hydrometer analysis for the finer fractions. This enabled us to classify the soil texture based on the percentages of sand, silt, and clay. Soil penetration resistance was measured in undisturbed soil using a digital cone penetrometer, which was equipped with a standard cone that had a 30° apex angle and a diameter of 12.83 mm. The penetrometer was inserted vertically at a constant rate of 30 mm/s to a depth of 150 mm—corresponding to the operating depth of the rotary blade—while recording the resistance at 10 mm depth increments. Soil salinity was evaluated by measuring the electrical conductivity of a 1:5 soil-water extract. Air-dried soil was mixed with distilled water in a 1:5 ratio, agitated for 30 minutes, and then allowed to settle. The electrical conductivity of the supernatant was subsequently measured using a Hanna Instruments HI2003-01 (Edge Multiparameter). A summary of the measured properties of the YRD soil is presented in Table 1.

Table 1

Physical and mechanical properties of the tested soil used in this study

Property	Value
Moisture content on a dry basis (%)	18.7
Wet bulk density (kg m^{-3})	1563
Cohesion (Pa)	23277
Sand (2–0.05 mm) (%)	43.3
Silt (0.05–0.002 mm) (%)	37.9
Clay (< 0.002 mm) (%)	18.8
Texture class	Loam

Property	Value
Penetration resistance at 150 mm depth (MPa)	1.82
Electrical Conductivity (dS·m^{-1})	1.23

5.1. Initialization and Stabilization of the Soil Material Model

A rectangular soil bin (2000 × 600 × 800 mm) was filled with simulated particles using a static factory. The particles were generated with a nominal diameter of 8 mm, with a random variation of ±5% (0.95 to 1.05 times the nominal size) to enhance packing density *(Aikins et al., 2021; El Salem et al., 2026)*. A total of 960,352 particles were randomly assigned positions and orientations within the bin using the 'fill section' option. To stabilize the initial particle arrangement across runs with varying input parameters, particles were created and arranged according to the initial parameter values listed in Table 2. The system was then subjected to a gravitational acceleration of -9.81 m/s² in the Z-direction and allowed to settle until stabilization. In this study, stabilization was defined as the point at which the total number of interparticle contacts ceased to increase (Figure 8). Finally, the depth of the soil bin was reduced to 250 mm for the subsequent chiseling simulation. A CAD model of the chisel shank was created in SolidWorks 2020 and subsequently imported into the EDEM simulation environment. During the simulation, the draft force was recorded over a 0.8 m travel distance under steady-state operating conditions (Figure 9).

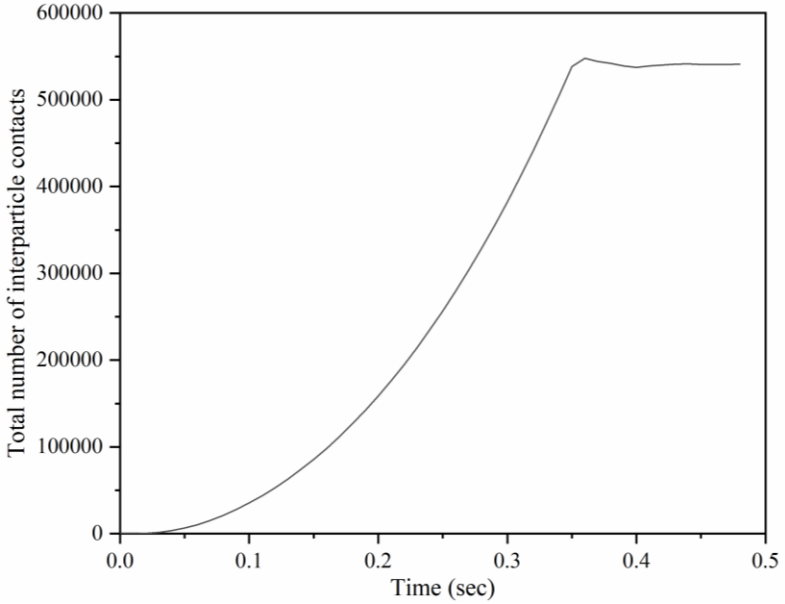

Fig. 8- Stability indicator of the particle assembly

Table 2

DEM input parameters applied for initial particle assembly generation and stabilization

(Bahrami et al., 2020; Cheng et al., 2023; El Salem et al., 2026; Ucgul et al., 2020; Zhang et al., 2025)

Property	Value
Poisson's ratio of the soil particle	0.37
Particle density (kg m^{-3})	2600
Shear modulus of soil particle (Pa)	1.82×10^{6}
Interparticle restitution coefficient	0.22
Soil-Soil internal friction coefficient	0.5
Soil-Soil rolling friction coefficient	0.28
The diameter of spherical particles (mm)	8
Particle size distribution	0.95 - 1.05
Poisson's ratio of steel	0.3
The density of steel (kg m^{-3})	7865
Shear modulus of steel (Pa)	7.9×10^{10}
Restitution coefficient of soil-steel	0.36

Property	Value
Soil-Steel external friction coefficient	0.5
Soil-Steel rolling friction coefficient	0.17
Damping factor	0.05
Stiffness factor	0.95
Soil Particle Yield Strength (Pa)	70000
Cohesive energy density of soil-soil (J m^{-3})	10540
Adhesive energy density of soil-steel (J m^{-3})	1500

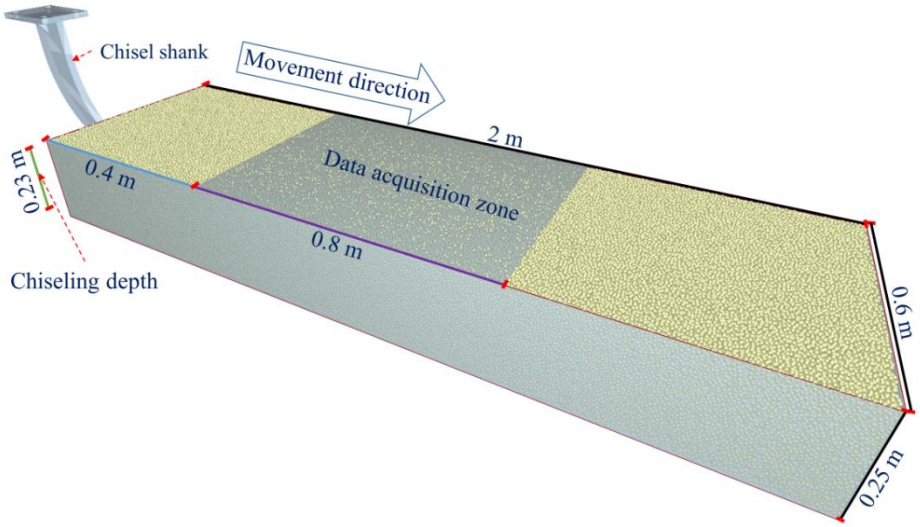

Fig. 9- A schematic diagram of the DEM simulation setup for the chiseling operation, illustrating the model geometry and the measurement zone

5.2. Sensitivity Analysis of Model Parameters

The Plackett-Burman (PB) experimental design is an efficient method for screening a large number of parameters to identify those with the greatest influence. This approach estimates the main effects of each parameter at two levels while requiring a minimal number of experimental runs, assuming that higher-order interactions are negligible. In this study, an 11-factor PB design was implemented to screen seven parameters of the proposed model, with the remaining four parameters assigned as virtual parameters to facilitate estimation of experimental error *(Xia et al., 2019)*. The DEM-simulated draft force of an individual chisel shank was used as the response variable. To ensure an equitable comparison and prevent the dominance of any single factor, the ratio of the high to low levels for each screened factor was kept at or below 2.5. The upper and lower limits for the screened parameters are detailed in Table 3. The Design Expert 10.0.4 software was utilized to set the testing settings, resulting in 12 simulation runs.

Table 3

Experimental parameters and their corresponding levels in the Plackett-Burman screening

Parameter	Symbol	Lower limit	Upper limit
Soil-soil static friction coefficient	X_1	0.4	0.7
Soil-soil rolling friction coefficient	X_2	0.15	0.3
Soil-steel static friction coefficient	X_3	0.3	0.6
Soil-steel rolling friction coefficient	X_4	0.15	0.35
Yield strength of the soil particle (Pa)	X_5	30000	70000
Cohesive energy density of soil-soil (J m-3)	X_6	7000	15000
Adhesive energy density of soil-steel (J m-3)	X_7	500	1200
Virtual parameters	A, B, C, D	-1	+1

5.3. Model and DEM Parameters Calibration

The key parameters influencing the draft force of a curved chisel shank were calibrated to match the experimentally measured draft force. This calibration process consisted of two sequential phases. In the first phase, a steepest-ascent experimental design was used to identify the approximate parameter range that could generate a simulated draft force matching the experimental value.

In the second phase, a Central Composite Design (CCD) was employed to optimize the parameters and develop a regression model, minimizing the relative error between simulated and experimental results *(Li et al., 2025)*. All simulations in this phase were conducted under the same operational conditions as the field test, specifically at a speed of 0.94 m/s and a depth of 0.22 m.

6. Operational Performance Assessment of the Developed Bio-Inspired Rotary Tiller Blade

The calibrated DEM model was used to systematically assess the performance of both conventional and bioinspired blades under various operational conditions. The experimental variables included blade shaft rotational speed (150-350 rpm) and tillage depth (60-140 mm).

The primary evaluation metric was the torque about the blade's rotational axis. For each experimental variable, a dedicated test series was conducted, systematically varying that parameter while keeping the other constant at predefined baseline levels (rotational speed: 240 rpm; tillage depth: 100 mm). All simulations were carried out at a constant forward speed of 0.5 m/s. This controlled, one-factor-at-a-time approach allowed for a direct performance comparison between the two blade designs across the specified operational ranges. In addition to torque, the disturbed soil area was used as a secondary evaluation index under these baseline parameters (0.5 m/s forward speed, 240 rpm, 100 mm depth).

RESULTS

1. Results of the DEM and contact model sensitivity analysis

The results of the Plackett–Burman screening test are presented in Tables 4 and 5. As outlined in Table 4, a sensitivity analysis determined that the soil-steel static friction coefficient is the most influential factor affecting the DEM-simulated draft force of the chisel shank. This positive correlation makes mechanistic sense: an increase in the friction coefficient increases shear resistance at the soil-shank interface, requiring greater force to overcome adhesion and initiate sliding. Consequently, this increases the total draft force. The next most influential parameters were the soil particle yield strength, interparticle cohesive energy density, interparticle static friction coefficient, and soil-steel adhesive energy density. Interestingly, the soil particle yield strength showed a negative correlation with draft force over the tested range, contradicting the usual expectation that higher yield strength increases shear resistance. This negative relationship can be explained by the role of the soil particle yield strength during the initial soil stabilization phase. A lower yield strength allowed for greater particle deformation, resulting in a final soil assembly with higher bulk density and more interparticle contacts. As a result, displacing this denser, more consolidated soil mass required a greater draft force to overcome its enhanced structural integrity. Finally, the two rolling friction coefficients (interparticle and soil-steel) were found to have negligible effects and were therefore held constant at 0.225 and 0.25, respectively, for all subsequent simulations. According to the Pareto chart analysis (Figure 10), parameters X1, X3, X5, and X6 have a strongly significant effect on the DEM-simulated draft force, as they exceed the Bonferroni-corrected significance level. Parameter X7 shows only a nominal significance, while Parameters X2 and X4 do not demonstrate any significant effect.

Table 4

Experimental design and results of the Plackett-Burman test

Run no.	X1	X2	X3	X4	X5	X6	X7	A	B	C	D	F
1	0.7	0.3	0.3	0.35	70000	15000	500	-1	-1	1	-1	571.3
2	0.4	0.3	0.6	0.15	70000	15000	1200	-1	-1	-1	1	674.6
3	0.7	0.15	0.6	0.35	30000	15000	1200	1	-1	-1	-1	970.3
4	0.4	0.3	0.3	0.35	70000	7000	1200	1	1	-1	-1	390.4
5	0.4	0.15	0.6	0.15	70000	15000	500	1	1	1	-1	592.7
6	0.4	0.15	0.3	0.35	30000	15000	1200	-1	1	1	1	612.2
7	0.7	0.15	0.3	0.15	70000	7000	1200	1	-1	1	1	406.1
8	0.7	0.3	0.3	0.15	30000	15000	500	1	1	-1	1	710.8
9	0.7	0.3	0.6	0.15	30000	7000	1200	-1	1	1	-1	811.7
10	0.4	0.3	0.6	0.35	30000	7000	500	1	-1	1	1	669.8
11	0.7	0.15	0.6	0.35	70000	7000	500	-1	1	-1	1	607.5
12	0.4	0.15	0.3	0.15	30000	7000	500	-1	-1	-1	-1	440.9

F represents the DEM-simulated draft force of an individual chisel shank.

Table 5

The order of influence of the calibrated parameters on the DEM-simulated draft force

Parameter	Effect	Sum of Squares	Contribution (%)	Influence ranking
X1	116.18	40495.7	13.19	4
X2	33.15	3296.77	1.07	6
X3	199.15	1.19 × 105	38.75	1
X4	30.78	2842.84	0.926	7
X5	-162.18	78910.3	25.7	2
X6	134.25	54069.19	17.61	3
X7	45.38	6178.94	2.01	5

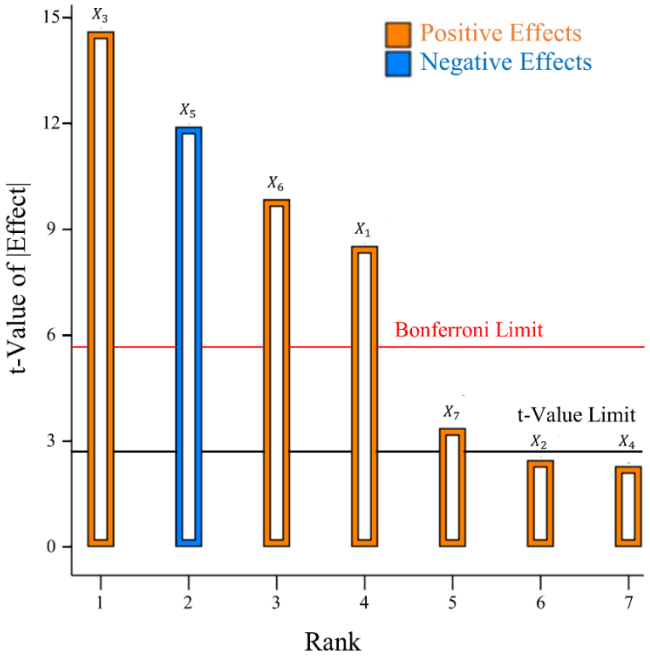

Fig. 10 - Pareto chart ranking the influence of the screened parameters on the DEM-simulated draft force of an individual chisel shank

2. Results of the proposed model calibration

2.1. Steepest Ascent Test Results

The Plackett-Burman screening test revealed that, among all screened parameters, the yield strength of soil particles is the only parameter negatively correlated with the DEM-simulated draft force. Based on this finding, a subsequent steepest ascent test was designed to incrementally increase the values of parameters X1, X3, X6, and X7 while systematically decreasing the value of parameter X5. This strategy aimed to identify the optimal range of the key influencing parameters that minimizes the relative error between the DEM-simulated and experimentally measured draft forces. The relative error between the DEM-simulated and experimentally measured draft forces was calculated for each simulation run. The design and results of the steepest ascent experiments are shown in Table 6. The findings revealed that the parameter values in run No. 4 resulted in the lowest relative error. Therefore, the parameter values from run No. 4 were taken as the middle values, while those from runs No. 3 and No. 5 served as the low and high values, respectively, for the subsequent Central Composite simulation test.

Table 6

Experimental design and results of the steepest ascent test

Trial no.	X1	X3	X5 (Pa)	X6 (J m^{-3})	X7 (J m^{-3})	F (N)	δF (%)
1	0.3	0.60	55000	2100	1800	523	26.5
2	0.4	0.65	50000	2200	1900	588	17.4
3	0.5	0.70	45000	2300	2000	655	8.0
4	0.6	0.75	40000	2400	2100	719	1.0
5	0.7	0.80	35000	2500	2200	803	12.8

2.2. Central Composite Test Results

Based on the steepest-ascent test's directional guidance, an orthogonal Central Composite Design (CCD) experiment was conducted to accurately identify the parameter set that minimizes the difference between the DEM-simulated draft force and the experimentally measured force. The design was analyzed using Design-Expert software and included five replications at the center point (m_0=5) and a star arm (α) value of 1.84 to ensure rotatability. Details on the coding of the experimental factors are provided in Table 7, while the complete design matrix and associated simulation results are presented in Table S1 (Supplementary Material). A regression model was developed to relate the DEM-simulated draft force to the independent variables using Design-Expert software. To simplify the model while maintaining its predictive power, insignificant terms were removed from the full quadratic model, yielding a refined quadratic polynomial (Equation 2). The statistical significance of the reduced quadratic polynomial model's terms, including main and interaction effects, was assessed using analysis of variance (ANOVA). The results of this analysis are summarized in Table 8.

$$F\,(N) = 822.78 + 375.53\,X_1 - 37.59\,X_3 - 66.2 \times 10^{-4}\,X_5 + 45.2 \times 10^{-3}\,X_6 - 6 \times 10^{-3}\,X_1X_5 \quad (2)$$

Table 7

Coded parameters and their corresponding levels for the central composite design (CCD)

Coded value	Calibrated parameters				
	X1	X3	X5 (Pa)	X6 (J m^{-3})	X7 (J m^{-3})
-α	0.42	0.66	30800	2216	1916
-1	0.50	0.70	35000	2300	2000
0	0.60	0.75	40000	2400	2100
1	0.70	0.80	45000	2500	2200
α	0.78	0.84	49200	2584	2284

The ANOVA results confirm the strength of the derived regression model. The model's P-value is highly significant (< 0.0001), indicating a strong relationship between the independent variables and the DEM-simulated draft force. Additionally, the non-significant lack-of-fit P-value (0.0892 > 0.05) suggests that the quadratic model fits the data well. The model's predictive strength is further illustrated by its near-unity coefficients of determination ($R^2 = 0.9899$, Adj. $R^2 = 0.9887$). The notably low coefficient of variation ($CV = 0.725\%$) and a high adequate precision value (101, which far exceeds the recommended threshold of 4) demonstrate the model's reliability and strong signal-to-noise ratio. As a result, this model is effective for predicting the DEM-simulated draft force without requiring additional simulation runs.

Table 8

Analysis of variance for the refined quadratic model of the Central Composite test

Variance Source	DF	Mean Square	F-Value	p-Value
Model	5	21933.15	805.84	< 0.0001*
X1	1	7123.22	261.71	< 0.0001*
X3	1	137	5.03	0.0303
X5	1	1.01×105	3722.74	< 0.0001*
X6	1	792.42	29.11	< 0.0001*
X1 X5	1	288	10.58	0.0023
Residual	41	27.22		
Lack of Fit	37	29.38	4.08	0.0892
Pure Error	4	7.2		
Total	46			

2.3. Determination of the Optimal Calibrated Parameter Set

The optimization of the refined quadratic polynomial model was conducted using the experimentally measured average draft force (712 N) as the target response variable, within the previously calibrated parameter ranges *(El Salem et al., 2026)*. By applying the numerical optimization function in Design-Expert software, the following optimal parameter values were determined: an interparticle static friction coefficient of 0.65, a soil-steel static friction coefficient of 0.74, a particle yield strength of 41402 Pa, an interparticle cohesive energy density of 2415 J/m³, and a soil-steel adhesive energy density of 2142 J/m³.

The rolling friction coefficients for interparticle and soil-steel interactions were maintained at their initial constant values of 0.225 and 0.25, respectively, as their influence was deemed negligible. Subsequently, this optimal parameter set was implemented in a DEM simulation, which yielded an average draft force of 697 N, corresponding to a relative error of 2.1% compared with the average experimental measurement of 712 N (Figure 11).

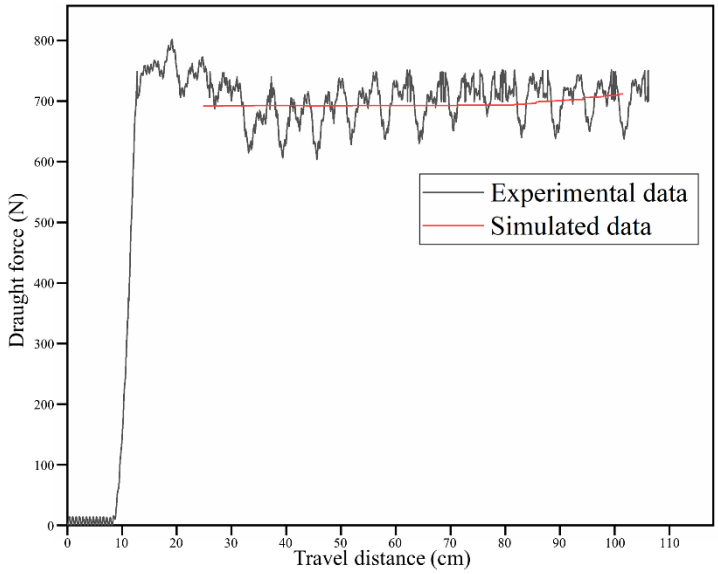

Fig. 11 - Comparison of experimental and simulated draught force data during a chiseling operation using the optimal calibrated parameter set

3. Effect of Operational Variables on DEM-simulated Blade Torque

The DEM-simulated blade torque values obtained from the single-factor test series are displayed in Table 9.

Table 9

Simulated torque on the blade's rotational axis across tested parameter levels

Parameter	Level	Mean torque (N.m)	
		Conventional IT-type blade	Bioinspired blade
Rotation Speed (rpm)	160	19.3	19.4
	200	28.1	25.2
	240	34.1	30.5
	280	41.5	36.7
	320	48.9	46.3
Tillage depth (mm)	60	26.1	24
	80	30.8	28.9
	100	34.1	30.5
	120	38.2	34.7
	140	39.6	36.8

3.1. Influence of Rotational Speed on Rotary Torque Demand

The impact of rotational speed on blade torque for both designs is shown in Figure 12. The data points represent the average values obtained from three simulation replicates at each rotational speed, conducted at a tillage depth of 100 mm and a forward speed of 0.5 m/s. As the rotational speed increased from 160 to 320 rpm, the torque required by both blades rose significantly. For the conventional blade, torque increased substantially from 19.5 N·m to 46.0 N·m. The bioinspired blade demonstrated a similar trend, with torque rising from 19.5 N·m to 44.0 N·m. Notably, while the torque values were the same at the lowest speed (160 rpm), the bioinspired blade consistently generated lower torque than the conventional blade at all higher speeds. The maximum observed difference was 3.0 N·m at 240 rpm. This consistent reduction in torque demand indicates that the bioinspired design maintains an energy efficiency advantage across the entire operational speed range, likely due to its optimized interaction with the soil medium, which reduces resistive forces during rotation.

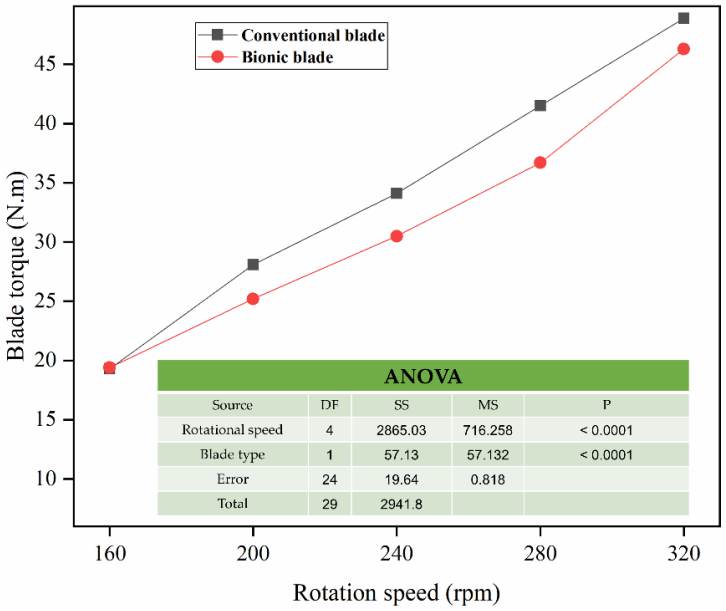

Fig. 12 - Variation of blade torque with rotational speed for conventional and bioinspired rotary blades.

3.2. Influence of Tillage Depth on Rotary Torque Demand

The data points shown in Figure 13 represent the mean values obtained from three simulation replicates at each tillage depth, conducted at a rotational speed of 240 rpm and a forward speed of 0.5 m/s. Statistical analysis of the effect of tillage depth revealed that tillage depth significantly influenced the torque of the rotary blades ($P < 0.0001$). For both the conventional and bioinspired blades, torque showed a strong positive correlation with tillage depth. The torque of the conventional blade increased by 50% (from 26.0 to 39.0 N·m) over the tested range of 60 to 140 mm, while the bioinspired blade's torque increased by 25% (from 24.0 to 30.0 N·m). More importantly, a highly significant main effect was observed for blade type ($P < 0.0001$), with the bioinspired blade generating substantially less torque at every depth. This performance difference was not constant but increased with depth: the torque reduction for the bioinspired blade was 7.7% at 60 mm, rising to 23.1% at 140 mm (Figure 13). This suggests that the bioinspired design not only reduces energy consumption but also demonstrates superior load-adaptive capability, maintaining greater efficiency under more demanding tillage conditions.

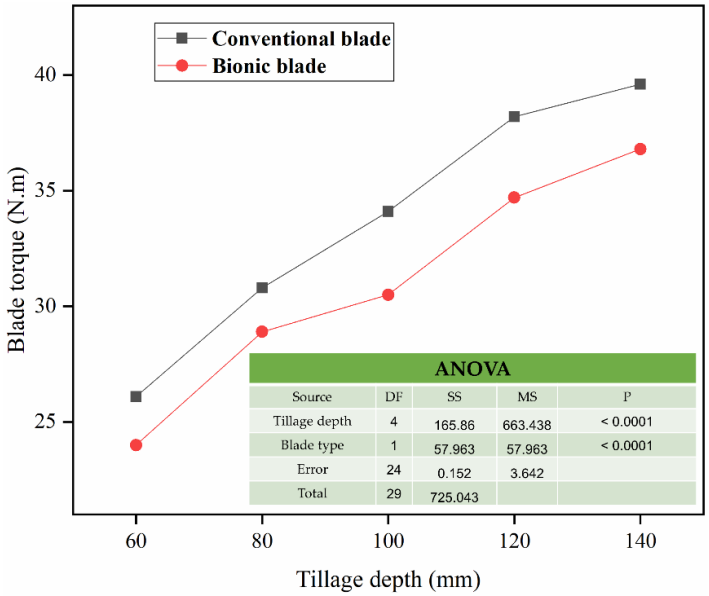

Fig. 13 - Blade torque versus tillage depth for the two blade designs, with associated ANOVA summary.

4. Impact of Blade Type on Disturbed Soil Area

In addition to torque, the disturbed soil area was used as a secondary evaluation index under these baseline parameters (0.5 m/s forward speed, 240 rpm, 100 mm depth).

This metric was quantified by analyzing the central longitudinal and cross-sectional soil profiles after the blade passed through. The boundary particles of the disturbed profile were identified by analyzing particle velocities immediately after the blade passed (Figure 14). The areas beneath the original soil surface were calculated using the trapezoidal rule for numerical integration, based on the coordinates of the boundary particles of the disturbed profile [25]. For two successive data points with coordinates (X_1, Z_1) and (X_2, Z_2), the area of each trapezoid was computed using the formula $((Z_1 + Z_2)/2) * (X_2 - X_1)$. The total area of the disturbed soil profile was obtained by summing the areas of all the individual trapezoids located within the disturbed profile (Figure 15). The simulation results show that the bio-inspired blade produced larger disturbed soil areas than the IT-type blade, with increases of 3.4% in the central longitudinal profile and 1.2% in the cross-sectional profile. To ensure a fair comparison, the bio-inspired blade was designed with the same rotational circumference as the conventional IT-type blade. However, the bio-inspired design features a more streamlined geometry, resulting in longer and narrower lateral extensions than those of the IT-type blade. This increased lateral reach likely contributed to the greater soil disturbance area observed with the bio-inspired blade.

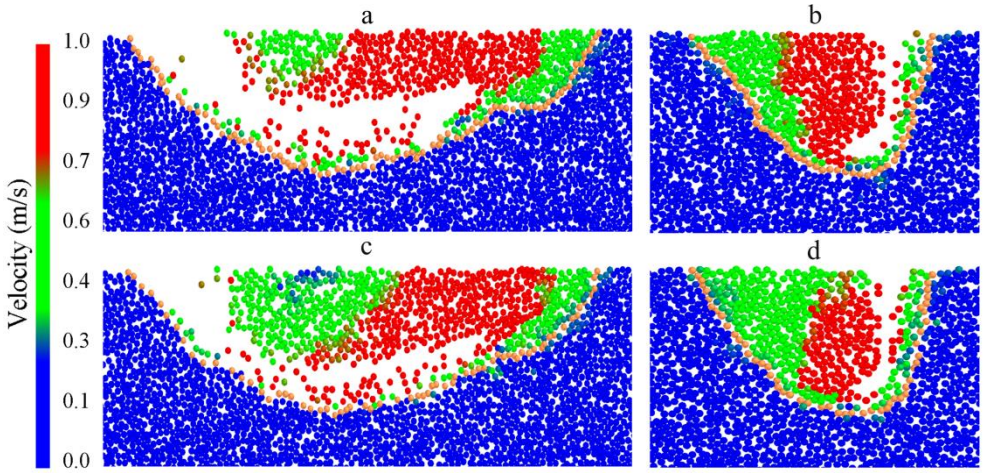

Fig. 14 - DEM-simulated results of disturbed soil areas: (a) IT-type blade, longitudinal profile; (b) IT-type blade, cross-sectional profile; (c) bio-inspired blade, longitudinal profile; (d) bio-inspired blade, cross-sectional profile

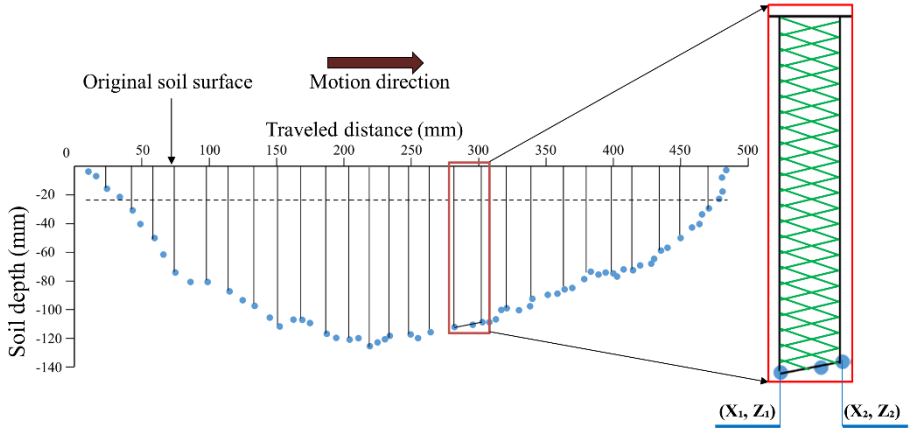

Fig. 15 - Calculation of the disturbed soil area using the trapezoidal rule for numerical integration

5. Comparative Study of an IT-Type Blade and a Bioinspired Rotary Blade in a Soil Bin

To assess the low soil-cutting resistance of the bioinspired rotary blade, a comparative experiment was conducted using a soil bin, with a conventional IT-type blade serving as the baseline. The IT-type blade, which features an Archimedes spiral cutting edge, is widely used in both paddy and dryland agriculture *(Cheng et al., 2023; Matin et al., 2021)*. The experiment was carried out under the following operational parameters: a rotational speed of 240 r/min, a forward speed of 0.5 m/s, and a plowing depth of 100 mm. Measurements showed that the bio-inspired blades reduced the average rotary torque on the rotating shaft by 17.8%. The torque decreased from 272.2 N·m for the IT-type blades to 223.7 N·m for the bio-inspired blades. This corresponds to average torques of 27.22 N·m per blade for the IT-type blades and 22.37 N·m per blade for the bio-inspired blades. In comparison, the simulated values per blade were 34.1 N·m for the IT-type blades and 30.5 N·m for the bio-inspired blades (Table 9).

This resulted in relative errors of 20.18% for the IT-type blades and 26.66% for the bio-inspired blades. These relatively high errors may be attributed to differences in testing conditions: the simulated values were obtained from a single blade operating in isolation, while the experimental results from the soil bin were derived from ten blades working simultaneously on a rotary shaft. To address this discrepancy, the simulation was repeated using the same blade configuration as the soil bin test, producing average per-blade torques of 29.71 N·m and 26.2 N·m. This resulted in substantially reduced relative errors of 12.9% for the IT-type blades and 14.1% for the bio-inspired blades. These findings demonstrate that the DEM model, together with the input parameters calibrated for the cohesive, salt-affected soil of this study, can reliably assess rotary plowing performance. The observed 17.8% reduction in average rotary torque for the bio-inspired blade compared to the conventional IT-type blade supports the idea that biomimetic designs can significantly reduce the energy demand of soil-engaging tools. This finding is consistent with previous studies documenting the low-resistance properties of biological structures. For example, *Sun et al., (2020)* reported that a ditcher inspired by bear claws exhibited lower specific energy consumption than a GB/T5996-2017 ditching blade, attributing this advantage to the optimized geometry of the claw. The torque reduction observed in our study is likely due to the gentle, curved cutting edge of the bio-inspired blade, which allows for smoother soil entry and a more uniform distribution of stress during rotary tillage. This design minimizes abrupt soil failure and decreases the peak cutting resistance encountered by the blade. As a result, lower torque demand directly translates into reduced power requirements for tillage operations. This offers a promising avenue for developing more energy-efficient agricultural machinery, especially in challenging soil conditions like those found in the Yellow River Delta. The reduction in torque, however, was accompanied by a slight decrease in soil fragmentation performance. The IT-type blades achieved a fragmentation rate of 89.1%, while the bio-inspired blades reached 85.6%, resulting in a difference of 3.9%. The higher fragmentation rate of the IT-type blade is likely due to its wider lateral flanges, which result in greater soil shearing and volumetric disturbance than the more streamlined bio-inspired design.

CONCLUSIONS

This study designed, simulated, and experimentally validated a bioinspired rotary tiller blade modeled after the claw morphology of the brown bear (Ursus arctos). The blade is specifically intended for use in cohesive, salt-affected soils in the Yellow River Delta. A novel biomimetic design was developed by extracting and scaling the claw's contours to reduce soil-cutting resistance while maintaining functionality equivalent to that of conventional IT-type blades. Using a systematically calibrated Discrete Element Method (DEM) model, which was refined through Plackett-Burman screening, steepest ascent tests, and Central Composite Design to align with experimental draft forces, simulations demonstrated that the bioinspired blade significantly reduced torque demand. This reduction reached up to 13% across rotational speeds (ranging from 160 to 320 rpm) and up to 11% across tillage depths (from 60 to 140 mm). Additionally, the blade produced a larger disturbed soil area, enhancing soil loosening. Soil bin experiments confirmed a 17.8% reduction in rotary torque for the bioinspired blade. In comparison, the conventional blade achieved a slightly higher soil fragmentation rate (3.9%) due to its wider flanges and more aggressive shearing action. This research validates that biomimetic principles derived from structures adapted for digging can lower energy consumption. The gentle, curved geometry of the blade promotes smoother soil entry and more uniform stress distribution. Additionally, it presents a calibrated DEM framework for simulating soil-tool interactions in salt-affected soils of the Yellow River Delta.

REFERENCES

[1] Aikins, K.A., Ucgul, M., Barr, J.B., Jensen, T.A., Antille, D.L., & Desbiolles, J.M.A. (2021). Determination of discrete element model parameters for a cohesive soil and validation through narrow point opener performance analysis. *Soil and Tillage Research*, 213, 105123. doi:https://doi.org/10.1016/j.still.2021.105123

[2] Bahrami, M., Naderi-Boldaji, M., Ghanbarian, D., Ucgul, M., & Keller, T. (2020). Simulation of plate sinkage in soil using discrete element modelling: Calibration of model parameters and experimental validation. *Soil and Tillage Research*, 203, 104700-104712.

[3] Bularda M., Vişinescu I, Ghiorghe A., Vlăduţ V., Cujbescu D. (2020). The effect of conservative agricultural works on soil and field plants and optimized mechanization technologies, *INMATEH – Agricultural Engineering*, vol. 61, no. 2, pp. 323-338, DOI: https://doi.org/10.35633/inmateh-61-35.

[4] Chen, X., Xu, G., Zhang, X., Tan, W., Ding, Q., & Tagar, A. A. (2024). Performance Evaluation of Biomimetic-Designed Rotary Blades for Straw Incorporation in an Intensive Tillage System. *Agriculture*, 14(8), 1426. Retrieved from https://www.mdpi.com/2077-0472/14/8/1426

[5] Cheng, J.; Xia, J.F.; Zheng, K.; Liu, G.Y.; Wei, Y.S.; Liu, Z.Y.; Li, P.L.; Liu, H.P. (2023). Construction and analysis of a discrete element model for calculating friction resistance of the typical rotary blades. *Computers and Electronics in Agriculture*, 214, 108303.

[6] Chertkiattipol, S., & Niyamapa, T. (2010). Variations of torque and specific tilling energy for different rotary blades. *International Agricultural Engineering Journal*, 19(3), 1-14.

[7] El Salem, A., Shang, S., Wang, D., Zhang, G., Wang, H., Abdeen, M. A., & Shehabeldeen, T. A. (2026). Developing an adequate DEM model to simulate soil-tool interactions under sticky soil conditions. *Soil and Tillage Research*, 256, 106893. doi: https://doi.org/10.1016/j.still.2025.106893

[8] El Salem, A., Zhang, G., Wang, H., Salem, H. M., Abdalla, M. A. I., & Ghazy, A. A. (2023). The effect of integrating a bio-inspired convex structure with a low-surface energy polymer on soil adhesion and friction. *Journal of Terramechanics*, 109, 93-100. doi: https://doi.org/10.1016/j.jterra.2023.06.003

[9] Fan, X., Liu, G., Tang, Z., & Shu, L. (2010). Analysis on main contributors influencing soil salinization of Yellow River Delta. *Journal of Soil and Water Conservation*, 24(1), 139-144.

[10] Godwin, R. J. (2007). A review of the effect of implement geometry on soil failure and implement forces. *Soil and Tillage Research*, 97(2), 331-340. doi: https://doi.org/10.1016/j.still.2006.06.010

[11] Hao, J. J., Yu, H. J., Zhao, J. G., Li, J. C., Ma, Z. K., & Cai, J. J. (2019). Design and test of wedge drag reduction rotary blade. *Transactions of the CSAE*, 35(8), 55-64.

[12] Li, B., Chen, Y., & Chen, J. (2016). Modeling of soil–claw interaction using the discrete element method (DEM). *Soil and Tillage Research*, 158, 177-185.

[13] Li, J. L., Li, C., Wu, Y. T., Cao, S. P., & Wang, M. H. (2023). The Grass Square Latch Paving Agency Based on the Bionic Spinning Knife. *Journal of Physics: Conference Series*. Vol. 2562, No.1, p.012060). IOP Publishing.

[14] Li, J., Zhang, J., Wang, Y., Zhang, H., Shen, S., Dong, W., & Abudu, S. (2025). Study on the Interaction Mechanism Between Sandy Soils and Soil Loosening Device in Xinjiang Cotton Fields Based on the Discrete Element Method. *Agriculture*, 15(24), 2587.

[15] Marsh, J.D.M., Rixon, A.J. (1991). Effects of heavy additions of organic residues on physical characteristics of three soil types in Queensland Australia. *Soil Tillage Res*. 20, 109–122. https://doi.org/10.1016/0167-1987(91)90129-L.

[16] Matin, M. A., Hossain, M. I., Gathala, M. K., Timsina, J., & Krupnik, T. J. (2021). Optimal design and setting of rotary strip-tiller blades to intensify dry season cropping in Asian wet clay soil conditions. *Soil and Tillage Research*, 207, 104854.

[17] Md-Tahir, H., Zhang, J., Xia, J., Zhang, C., Zhou, H., & Zhu, Y. (2019). Rigid lugged wheel for conventional agricultural wheeled tractors – Optimising traction performance and wheel–soil interaction in field operations. *Biosystems Engineering*, 188, 14-23.

[18] Qin, Y., Gao, Y., Xie, C., Tong, J., Wang, Q., & Feng, X. (2025). Design and Test of an Energy-Saving Bionic-Inspired Rotary Blade: A Study on Power Consumption and Soil Surface Quality. *Agriculture*, 15(9), 938.

[19] Salem, A. E., Wang, H., Gao, Y., Zha, X., Abdeen, M. A., & Zhang, G. (2021). Effect of Biomimetic Surface Geometry, Soil Texture, and Soil Moisture Content on the Drag Force of Soil-Touching Parts. *Applied Sciences*, 11(19), 8927-8938.

[20] Siddique, K.H.M.; Johansen, C.; Turner, N.C.; Marie-Hélène, J.M.H.; Hashem, A.; Sakar, D.; Gan, Y.; Alghamdi, S.S. (2012). Innovations in agronomy for food legumes. A review. *Agronomy for sustainable development*, 32(1), 45-64.

[21] Sun, J., Chen, H., Wang, Z., Ou, Z., Yang, Z., liu, Z., & Duan, J. (2020). Study on plowing performance of EDEM low-resistance animal bionic device based on red soil. *Soil and Tillage Research*, 196, 104336.

[22] Sun, J., Wang, Y., Ma, Y., Tong, J., & Zhang, Z. (2018). DEM simulation of bionic subsoilers (tillage depth >40 cm) with drag reduction and lower soil disturbance characteristics. *Advances in Engineering Software*, 119, 30-37.

[23] Ucgul, M., & Saunders, C. (2020). Simulation of tillage forces and furrow profile during soil-mouldboard plough interaction using discrete element modelling. *Biosystems Engineering*, 190, 58-70.

[24] Ucgul, M., Fielke, J. M., & Saunders, C. (2015). Three-dimensional discrete element modelling (DEM) of tillage: Accounting for soil cohesion and adhesion. *Biosystems Engineering*, 129, 298-306.

[25] Ungureanu N., Croitoru Şt., Biriş S., Voicu Gh., Vlăduţ V., Selvi K.Ç., Boruz S., Marin E., Matache M., Manea D., Constantin G., Ionescu M. (2015). Agricultural soil compaction under the action of agricultural machinery, *Proceedings of the 43 international Symposium on Agricultural Engineering "Actual Tasks on Agricultural Engineering*", pp. 31-42.

[26] Vlăduţ D.I., Biriş S., Vlăduţ V., Cujbescu D., Ungureanu N., Găgeanu I (2018). Experimental researches on the working process of a seedbed preparation equipment for heavy soils, *INMATEH – Agricultural Engineering*, vol. 55, no. 2, pp. 27-34.

[27] Vlăduţoiu L., Cârdei P., Vlăduţ V., Fechete L. (2017). Modern trends in designing and selecting the machine / equipment for soil deep tillage, *16th International Scientific Conference "Engineering for Rural Development*", pp. 1415-1420.

[28] Vlăduțoiu L.C., Chişiu G., Tudor A., Vlăduț N-V., Fechete-Tutunaru L., Marin E., Grigore I-A. (2023). Tribological study of chisel knives of soil tillers, *Agriculture* 13(6): 11235, agriculture-2426368; DOI:10.3390/agriculture13061235.

[29] Xia, R., Li, B., Wang, X., Li, T., & Yang, Z. (2019). Measurement and calibration of the discrete element parameters of wet bulk coal. *Measurement*, 142, 84-95.

[30] Xie, C., Wei, W., Zhu, Y., Xiao, M., & Chen, T. (2025). Wear reduction damage mitigation and operational reliability analysis of rotary tiller knives based on the self-excited vibration theory. *Computers and Electronics in Agriculture*, 231, 109991.

[31] Xiong, P., Yang, Z., Sun, Z., Zhang, Q. Q., Huang, Y. Q., & Zhang, Z. W. (2018). Simulation analysis and experiment for three-axis working resistances of rotary blade based on discrete element method. *Transactions of the CSAE*, 34(18), 113-121.

[32] Xiong, P., Yang, Z., Sun, Z., Zhu, Q., Zhu, Z., & Gu, Y. (2017). Experiment on three-axis working resistances of rotary blade and working parameters optimization. *Transactions of the Chinese Society of Agricultural Engineering*, 33(19), 51-58.

[33] Yang, Y. W., Tong, J., Ma, Y. H., Jiang, X. H., & Li, J. G. (2019). Design and experiment of biomimetic rotary tillage blade based on multiple claws characteristics of mole rats. *Trans. Chin. Soc. Agric. Eng*. 35(19), 37-45.

[34] Zhang, F., Luo, Z., Zheng, E., Han, L., Qian, J., Yao, H., Shi, Y., Wang, X. (2025). Imitating pangolin scale structure for reducing adhesion and resistance of rotary tillage in wet-adhesive soil. *Soil and Tillage Research*, 245, 106306.

[35] Zheng, S., Lu, T., Liu, J., Tian, Y., Han, M., Tai, M., Gao, S., Liu, T., Wang, D., Zhao, Z. (2025). Discrete Element-Based Design of a High-Speed Rotary Tiller for Saline-Alkali Land and Verification of Optimal Tillage Parameters. *Agriculture*, 15(3), 269.

[36] Zhihong, Z., Xiaoyang, W., Jin, T., & Carr, S. (2018). Innovative Design and Performance Evaluation of Bionic Imprinting Toothed Wheel. *Applied Bionics and Biomechanics*, 2018, 1-11.